The Astrophysical Journal, 780:95 (14pp), 2014 January 1 doi:10.1088/0004-637X/780/1/95

THE IMPACT OF UPDATED Zr NEUTRON-CAPTURE CROSS SECTIONS AND NEW ASYMPTOTIC GIANT BRANCH MODELS ON OUR UNDERSTANDING OF THE *S* PROCESS AND THE ORIGIN OF STARDUST

Maria Lugaro[1], Giuseppe Tagliente[2,8], Amanda I. Karakas[3], Paolo M. Milazzo[4], Franz Käppeler[5], Andrew M. Davis[6,9,10], and Michael R. Savina[7,9]
[1] Monash Centre for Astrophysics (MoCA), Monash University, Clayton, VIC 3800, Australia; maria.lugaro@monash.edu
[2] Istituto Nazionale di Fisica Nucleare (INFN), Bari, Italy; giuseppe.tagliente@ba.infn.it
[3] Research School of Astronomy and Astrophysics, Australian National University, Canberra, ACT 2611, Australia; amanda.karakas@anu.edu.au
[4] Istituto Nazionale di Fisica Nucleare (INFN), Trieste, Italy; paolo.milazzo@ts.infn.it
[5] Karlsruhe Institute of Technology, Campus North, D-76021 Karlsruhe, Germany; franz.kaeppeler@kit.edu
[6] The Department of the Geophysical Sciences, The University of Chicago, Chicago, IL 60637, USA; a-davis@uchicago.edu
[7] Materials Science Division, Argonne National Laboratory, Argonne, IL 60439, USA; msavina@anl.gov
Received 2013 August 5; accepted 2013 November 11; published 2013 December 13

ABSTRACT

We present model predictions for the Zr isotopic ratios produced by *slow* neutron captures in C-rich asymptotic giant branch (AGB) stars of masses 1.25–4 $M_{\odot}$ and metallicities $Z = 0.01$–0.03, and compare them to data from single meteoritic stardust silicon carbide (SiC) and high-density graphite grains that condensed in the outflows of these stars. We compare predictions produced using the Zr neutron-capture cross sections from Bao et al. and from n_TOF experiments at CERN, and present a new evaluation for the neutron-capture cross section of the unstable isotope ^{95}Zr, the branching point leading to the production of ^{96}Zr. The new cross sections generally present an improved match with the observational data, except for the ^{92}Zr/^{94}Zr ratios, which are on average still substantially higher than predicted. The ^{96}Zr/^{94}Zr ratios can be explained using our range of initial stellar masses, with the most ^{96}Zr-depleted grains originating from AGB stars of masses 1.8–3 $M_{\odot}$ and the others from either lower or higher masses. The ^{90,91}Zr/^{94}Zr variations measured in the grains are well reproduced by the range of stellar metallicities considered here, which is the same needed to cover the Si composition of the grains produced by the chemical evolution of the Galaxy. The ^{92}Zr/^{94}Zr versus ^{29}Si/^{28}Si positive correlation observed in the available data suggests that stellar metallicity rather than rotation plays the major role in covering the ^{90,91,92}Zr/^{94}Zr spread.

Key words: nuclear reactions, nucleosynthesis, abundances – stars: AGB and post-AGB

Online-only material: color figures

1. INTRODUCTION

Stardust grains are tiny ($\sim\mu$m) specks of dust extracted from primitive meteorites for which laboratory analysis has revealed isotopic compositions of many elements completely different from those of the bulk of solar system material. Large isotopic anomalies in an extended list of elements cannot be wrought by chemical fractionation only but primarily must be produced by nuclear reactions, which means that stardust grains carry the signature of their formation environments around different types of astrophysical objects, from giant stars to novae and supernovae. Different types of stardust grains have been recovered to date including diamond, graphite, silicon carbide, silicon nitride, and various types of oxides and silicates. See Clayton & Nittler (2004), Zinner (2008), and Davis (2011) for reviews, and Lugaro (2005) for a textbook on the topic.

Stardust silicon carbide (SiC) grains were discovered in 1987 (Bernatowicz et al. 1987) and have been the most extensively studied type of stardust. This is because they are easier to extract from meteoritic rocks than other types of grains and have relatively large sizes, up to several microns, which makes them more manageable in the laboratory. Virtually all SiC grains have a stellar origin owing to the fact that SiC can only form in C-rich gas (i.e., C/O > 1), whereas in the solar system C/O $\sim$ 0.5. The vast majority of stardust SiC grains ($\sim$93%, also referred to as "mainstream" SiC) originate from the condensation of gas into solid in the outer layers of the envelopes of C-rich asymptotic giant branch (AGB) stars of approximately solar metallicity and were ejected into the surrounding interstellar medium by strong stellar winds. Several lines of evidence point to the C-rich AGB origin for mainstream SiC stardust and have been extensively discussed before (e.g., Gallino et al. 1990; Hoppe & Ott 1997; Lugaro et al. 1999). In summary: SiC molecules need a C-rich gas to form, as mentioned above, and their emission line at 11.2 μm is observed in the infrared spectra of C-rich AGB stars (see, e.g., Speck et al. 1999); the distribution of the ^{12}C/^{13}C ratio of mainstream SiC grains matches that of C-rich AGB stars; the Ne isotopic signature, with large excesses in ^{22}Ne, is also explained, as this isotope is a main product of He burning in AGB stars. The distribution of Si (and Ti) shows excesses up to 20% in the neutron-rich isotopes, i.e., the ^{29,30}Si/^{28}Si ratios are up to 20% higher than solar and can be explained by the combined effect of the chemical evolution of the Galaxy, stellar migration, inhomogeneities in the interstellar medium, and increased condensation efficiency of SiC dust with increasing stellar metallicity (Lewis et al. 2013) or a Galactic merger event (Clayton 2003). Another unmistakable signature of AGB nucleosynthesis in mainstream SiC grains is the presence of elements heavier than iron with isotopic compositions typical of the *slow* neutron-capture process (the *s*-process; Lugaro et al. 2003a, hereafter LDG03). This is well known to occur in AGB stars as enhancements in *s*-process elements, such as Sr, Y, Zr, Ba, and Nd, are spectroscopically observed (e.g., Smith & Lambert 1989). The *s*-process isotopic signature in SiC has been confirmed for several elements: Kr, Sr, Zr, Mo,

[8] Also at University of Ghent, Ghent, Belgium.
[9] Also at Chicago Center for Cosmochemistry, USA.
[10] Also at The Enrico Fermi Institute, The University of Chicago, Chicago, IL 60637, USA.

Ba, Xe, Nd, Sm, Dy (see, e.g., Nicolussi et al. 1997; Gallino et al. 1997 and literature therein), and recently Eu (Ávila et al. 2013b), W (Ávila et al. 2012b), and Pb (Ávila et al. 2012a). The historical discovery of the radioactive element Tc in AGB stars by Merrill (1952)—which first demonstrated the occurrence of in situ nucleosynthesis processes in stars— was also confirmed by measurements of excesses in ^{99}Ru in stardust SiC grains due to the radioactive decay of ^{99}Tc, which is on the *s*-process path (Savina et al. 2004).

The origin of stardust graphite grains, on the other hand, is controversial and several stellar sources have been proposed. Low-density graphite grains show the signature of formation in the ejecta of core-collapse supernovae (see, e.g., Travaglio et al. 1999; Pignatari et al. 2013b), while high-density graphite grains appear to have originated in several different stellar sources: core-collapse supernovae, born-again post-AGB stars, and C-rich AGB stars with metallicity lower than solar (Jadhav et al. 2008). Nicolussi et al. (1998) discovered an *s*-process signature in the Zr composition of six high-density graphite grains, most likely coming from internal carbides extremely enriched by the *s*-process (Croat et al. 2005), strengthening the link between these grains and AGB stars.

1.1. The s-process in AGB Stars

The *s*-process occurs in the deep He-rich region of AGB stars. This region is usually referred to as the "intershell" because it is found between the He-burning shell, located on top of the degenerate C–O core, and the H-burning shell, located below the extended H-rich convective envelope. Hydrogen and helium burning occur alternately in AGB stars. The H-burning shell is active most of the time, while the He-burning shell turns on episodically when enough H has been converted into He so that the bottom layers of the intershell are compressed and heated up. Under these conditions, He burning suddenly releases a large amount of energy, which drives convective motion in the whole intershell (the thermal pulse, TP). This causes expansion and cooling of the whole stellar structure and the quenching of both the H-burning shell and, eventually, the He-burning shell. At this point the star contracts again, H burning resumes, and a new cycle of alternate H and He burning begins (see Herwig 2005 for a review). After each TP, a "third dredge-up" (TDU) episode may occur, which carries to the convective envelope (and to the stellar surface) the products of partial He burning, including ^{12}C, ^{22}Ne, and *s*-process elements. For detailed models of the *s*-process in AGB stars, we refer to Gallino et al. (1998), Busso et al. (1999), Goriely & Mowlavi (2000), Lugaro et al. (2003b), Straniero et al. (2006), Cristallo et al. (2009b), Bisterzo et al. (2010), and Lugaro et al. (2012). Here, we provide a brief description.

Two neutron sources are active in the intershell: the ^{13}C(α, n)^{16}O and the ^{22}Ne(α, n)^{25}Mg reactions. Neon-22 is produced via double α-capture on ^{14}N, which is very abundant in the H-burning ashes ingested in the TPs, and burns via (α, n) reactions inside the convective TPs if the temperature reaches 300 MK (∼26 keV), producing a neutron flux over a short time (a few years) characterized by high neutron densities, up to 10^{15} cm^{-3}. The ^{22}Ne neutron source is the main neutron source in massive AGB stars (above ∼4 $M_{\odot}$) that experience high temperature in their TPs (Truran & Iben 1977; van Raai et al. 2012; Karakas et al. 2012; D'Orazi et al. 2013). In low-mass AGB stars (below ∼4 $M_{\odot}$) the ^{22}Ne neutron source is only marginally activated and ^{13}C nuclei are the neutron source. To have enough ^{13}C nuclei to reproduce the observational constraints, it is assumed that some mixing of protons occurs from the envelope into the intershell at the end of each TDU episode. These protons react with the abundant ^{12}C to produce a region rich in ^{13}C (the ^{13}C *pocket*), which burns via (α, n) reactions typically in radiative conditions before the onset of the next TP (i.e., during the periods in between TPs, "interpulses") at temperatures of ∼90 MK (∼8 keV), releasing a neutron flux over a relatively long period of time (∼10^4 yr).

By comparing the composition of Sr, Zr, Mo, and Ba from AGB stars and mainstream SiC grains, LDG03 concluded that most of these grains should have condensed in low-mass AGB stars. This is because the high neutron densities in massive AGB stars activate branching points on the *s*-process path and produce isotopic ratios shifted toward the neutron-rich isotopes, resulting in isotopic signatures that are not observed in the grains. This conclusion is in agreement with the fact that massive AGB stars experience proton-capture nucleosynthesis at the base of the convective envelope (hot bottom burning; Boothroyd et al. 1993), which converts C into N and prevents the formation of C-rich gas—the necessary condition for the formation of SiC. For this reason, in the present paper we restrict our discussion to models of low-mass AGB stars that become C-rich and where ^{13}C is the main neutron source. Above this mass, our models experience efficient hot bottom burning, which prevents them from becoming C-rich (Karakas 2010).

1.1.1. Current Issues with the s-process in Low-mass AGB Stars

As mentioned above, many observational studies show that low-mass AGB stars are *s*-process enhanced, and the source of free neutrons in these stars is assumed to be ^{13}C nuclei. However, the mechanism for the production of the ^{13}C nuclei is not well known because it depends on the treatment of convective borders in stars (see discussion in Busso et al. 1999). Accurate modeling requires three-dimensional hydrodynamical simulations of the interface between the envelope and the intershell of AGB stars, which are not available yet. In one-dimensional AGB models, a ^{13}C pocket is artificially introduced by assuming the existence of some partial mixing of protons from the envelope into a thin layer at the top of the intershell at the end of each TDU episode. This is under the assumption that the mixing leading to the formation of the ^{13}C pocket can occur only once the TDU has produced a sharp discontinuity between the convective envelope and the radiative intershell. Free parameters allow us to adjust the features of the mixing zone in order to match the observations (e.g., Goriely & Mowlavi 2000; Cristallo et al. 2009b; Bisterzo et al. 2010; Lugaro et al. 2012). On top of the missing knowledge regarding the formation mechanism of the ^{13}C pocket, there are a number of further problems associated with this *s*-process scenario.

1. While in most cases the ^{13}C pocket completely burns before the onset of the following TP, in stars of mass lower than ∼2 $M_{\odot}$, the temperature may be low enough that a significant fraction of ^{13}C is left in the pocket at the time of the ingestion in the following TP (Cristallo et al. 2009b; Lugaro et al. 2012). This ^{13}C burns convectively inside the TP, which results in (1) decreasing the overall neutron exposure (i.e., the total number of free neutrons) due to the presence of ^{14}N ingested in the TP from the H-burning ashes, a strong neutron poison via the ^{14}N(n, p)^{14}C reaction, and (2) increasing the neutron density due to the shorter burning timescale (see discussion in Guo et al. 2012). This preferentially occurs in the first stages of the thermally pulsing AGB phase, because the star heats up

as it evolves. It should be noted that the occurrence of this ^{13}C ingestion in the TP is strictly connected to the uncertainties related to the occurrence of the TDU at these very low masses: in the current scenario, AGB stars will form a ^{13}C pocket only if they experience the TDU, and the lowest mass at which AGB stars experience the TDU is unknown, extremely model dependent (Frost & Lattanzio 1996; Mowlavi 1999; Stancliffe & Jeffery 2007), and poorly constrained by observations (Wallerstein & Knapp 1998).

2. All stars rotate, but the effect of rotation on the *s*-process is still very poorly determined. The angular velocity profile inside AGB stars may present a steep discontinuity between the contracting core and the expanding envelope and result in mixing inside the ^{13}C pocket, which carries the ^{14}N neutron poison into the ^{13}C-rich layers and lowers the neutron exposure (Herwig et al. 2003; Siess et al. 2004; Piersanti et al. 2013). Effects such as magnetic fields (Suijs et al. 2008) and gravity waves can modify the evolution of the angular momentum in the star and may reduce the difference in the angular velocity between the core and the envelope; these effects have not been considered in *s*-process studies so far.
3. Overshoot at the bottom of the TP can lead to increased temperatures and activation of the ^{22}Ne neutron source in the low-mass AGB models—together with an increase of the amount of ^{12}C in the intershell—resulting in higher neutron exposures in the ^{13}C pocket than models without overshoot (Herwig 2000; Lugaro et al. 2003b). While it has been shown that this overshoot in a 3 $M_{\odot}$ star produces *s*-process predictions that do not agree well with observations, including constraints from Zr in stardust (Lugaro et al. 2003b), a comprehensive study is not yet available. Recent models by Pignatari et al. (2013a) include such overshoot into a 1.5 $M_{\odot}$ star, which will allow further analysis of this effect.
4. Finally, there is another possibility for the formation of the ^{13}C neutron source. Protons may be ingested directly at the top of the TPs, in which case the neutrons for the *s*-process are all released in the convective region (Cristallo et al. 2009a; Lugaro et al. 2012). This process along with the mass and metallicity range where it occurs is very uncertain as it again depends on the treatment of convective borders in stars. In this case, the first multidimensional simulations are available to guide the one-dimensional models (Stancliffe et al. 2011; Herwig et al. 2011, 2013).

While some progress has been achieved in the modeling of these potential effects, their significance on our overall understanding of the *s*-process has not yet been pinned down, and their impact on the interpretation of observational constraints is unclear. In the following, we will use Zr in stardust to address points 1 and 2 above, and discuss possible implications of point 3. Point 4 requires parametric models of proton-ingestion episodes, which we plan for future work.

1.1.2. s-process Zr from AGB Stars and Stardust Grains

Zr is a typical *s*-process element belonging to the first *s*-process peak in the solar-abundance distribution (predicted *s*-process contributions to its solar abundance range from ∼70% to ∼90%; Arlandini et al. 1999; Goriely 1999; Travaglio et al. 2004; Sneden et al. 2008). Comparison of predictions of the isotopic abundances of Zr to stardust data are critical to constrain the *s*-process in AGB stars and to identify the range of masses and metallicities of the SiC parent stars. The path of neutron captures along the Zr isotopes has been discussed in detail in LDG03 (see Figure 1 and Section 8 of that paper) and will not be repeated here. Several of the Zr isotopes have close to the magic number of neutrons ($N = 50$)—^{90}Zr has exactly $N = 50$—which results in the relative production of ^{90,91,92,94}Zr being extremely sensitive to the overall neutron exposure. On the other hand, the abundance of the remaining stable isotope, ^{96}Zr, is determined by the neutron density because its production is driven by the activation of the branching point at the unstable ^{95}Zr with a half-life of 64 days (and no dependence on the temperature). It should be noted that the ^{90,91}Zr/^{94}Zr ratios may also be somewhat affected by the branching points at the unstable ^{89,90}Sr and ^{91}Y (see LDG03), which are uncertain given that their neutron-capture cross sections have been determined only theoretically. Finally, most of the abundance of the element Nb is due to the radiogenic decay of the long-lived ^{93}Zr (half-life = 1.5 Myr, down to 0.3 Myr at 300 MK; see Takahashi & Yokoi 1987).

In LDG03, the comparison of AGB predictions to the Zr composition of single SiC data presented some problems: it was not possible to match the few grains that exhibit an extreme deficit of ^{96}Zr, and the ^{90}Zr/^{94}Zr and ^{92}Zr/^{94}Zr ratios in some grains were higher than predicted. LDG03 argued that improved measurements of neutron-capture cross sections for the Zr isotopes may be a key to solving these problems. Such improved estimates are now available as the neutron-capture cross section of all the stable Zr isotopes and the long-lived ^{93}Zr have been recently remeasured with high precision at the neutron time of flight (n_TOF) facility at CERN (see Section 2 and Tagliente 2008a, 2008b; Tagliente et al. 2010, 2011a, 2011b, 2013). Furthermore, the Zr data set for single SiC grains has been extended by Barzyk et al. (2007) since the analysis presented in LDG03.

The aim of this paper is to present updated predictions for the Zr isotopic composition produced by the *s*-process in AGB stars resulting from the most recent estimates of the neutron-capture cross sections (Section 2) and new AGB models (Section 3). By comparing the revised predictions to the composition observed in SiC and graphite grains, we hope to reach a better understanding of the operation of the *s*-process in low-mass AGB stars and of the mass and metallicity of the AGB parent stars of SiC and graphite grains (Section 4). Our findings and future prospects are summarized in Section 5.

2. NEUTRON-CAPTURE CROSS SECTIONS OF THE Zr ISOTOPES

The Maxwellian-averaged cross sections (MACS) used in the calculations presented in LDG03 were taken from the compilation of Bao et al. (2000) and were based on experimental data that had been mainly obtained from pioneering experiments performed in the 1970s (Bartolome et al. 1969; Boldeman et al. 1975, 1976; Musgrove et al. 1977; Coceva et al. 1979). These data are in general incomplete and in some cases present large discrepancies.

In 2002 May, the n_TOF became fully operational at CERN with the aim of making neutron capture and fission measurements with high accuracy over a wide energy range (Rubbia et al. 1998; Borcea et al. 2003). The facility delivers neutrons produced by spallation reactions induced by a pulsed 20 GeV c^{-1} proton beam. The main characteristic of n_TOF is the high instantaneous neutron flux in combination with a low duty cycle, high neutron energy resolution, and low background; this allows it to collect neutron-capture cross section data with

Table 1
Reaction Rates $N_A < \sigma v >$ of (n, γ) Reactions of the Stable Zr Isotopes and the Unstable ^{93}Zr and ^{95}Zr, all Given in Units of 10^6 cm^3 mole^{-1} s^{-1}

					^{90}Zr						
kT (keV)	5	10	15	20	25	30	40	50	60	80	100
Bao et al.	2.54	2.84	2.96	2.95	3.03	3.04	3.00	3.17	3.27	3.54	3.69
This work	2.62	2.61	2.64	2.68	2.73	2.79	2.85	2.89	2.92	2.93	2.90
					^{91}Zr						
kT (keV)	5	10	15	20	25	30	40	50	60	80	100
Bao et al.	15.0	12.3	10.7	9.80	9.12	8.68	8.18	8.03	7.97	8.02	8.44
This work	14.0	12.0	10.8	10.1	9.50	9.11	8.51	8.21	7.77	7.79	7.39
					^{92}Zr						
kT (keV)	5	10	15	20	25	30	40	50	60	80	100
Bao et al.	7.74	6.43	5.63	5.20	4.89	4.77	4.67	4.85	5.10	5.42	6.06
This work	8.00	6.72	6.02	5.68	5.51	5.46	5.54	5.71	5.91	6.35	6.78
					^{93}Zr						
kT (keV)	5	10	15	20	25	30	40	50	60	80	100
Bao et al.	20.1	17.8	16.6	15.6	14.6	13.8	12.5	11.6	11.1	10.4	9.78
This work	20.0	17.9	16.5	15.5	14.5	14.1	13.5	11.9	12.2	11.6	11.3
					^{94}Zr						
kT (keV)	5	10	15	20	25	30	40	50	60	80	100
Bao et al.	4.37	4.34	4.09	3.90	3.83	3.76	3.84	4.28	4.69	4.95	5.53
This work	4.15	4.36	4.32	4.31	4.34	4.41	4.57	4.75	4.97	5.33	5.70
					^{95}Zr						
kT (keV)	5	10	15	20	25	30	40	50	60	80	100
Bao et al.	17.5	15.4	13.9	12.9	12.0	11.4	10.5	10.1	9.62	9.21	8.98
This work	15.1	8.94	6.75	5.47	4.65	4.11	3.57	3.03	3.05	2.92	2.86
					^{96}Zr						
kT (keV)	5	10	15	20	25	30	40	50	60	80	100
Bao et al.	3.31	2.34	1.95	1.65	1.58	1.55	1.39	1.27	1.19	1.04	0.93
This work	3.13	2.18	1.77	1.52	1.37	1.28	1.21	1.21	1.25	1.34	1.45

Notes. Uncertainties are ∼5% at 1σ for all the isotopes, except ^{95}Zr, whose cross section is derived empirically and has a larger associated uncertainty.

improved accuracy and with an excellent signal-to-background ratio. Given the high quality of n_TOF, dedicated detectors were developed. Deuterated benzene (C_6D_6) γ-ray detectors contained in a cylindrical low-mass carbon fiber housing (Plag et al. 2003) have been used for neutron-capture measurements. These detectors are well suited for accurate measurements of resonance-dominated (n, γ) cross sections, e.g., of light and neutron-magic isotopes. The samples were kept in position by a carbon-fiber sample-changer. The mass of the experimental setup was reduced as much as possible and materials such as deuterium, carbon, oxygen, and silicon were chosen as the main constituents of the scintillator and the detectors because they present very low neutron-capture cross sections. Moreover, the analysis of n_TOF data benefits from the performance of modern data acquisition techniques with fast digitizers, which allows us to analyze the data offline in the most flexible way, including an efficient pulse shape analysis for n/γ discrimination. Other developments relate to the use of the well-tested and advanced R-matrix code SAMMY (Larson 2006). The recent n_TOF data present, in general, lower capture cross sections than previous experiments. This can be explained in terms of the more advanced experimental instrumentation and software for offline data analysis. The main improvement is certainly related to the strong reduction of neutron sensitivity, i.e., the background induced by neutrons scattered by the sample and captured in the materials constituting the experimental setup.

A full campaign of n_TOF measurements was dedicated to the Zr stable isotopes and the long-lived unstable isotope ^{93}Zr. The neutron sensitivity of the capture setup was particularly important in the Zr measurements, considering the large scattering-to-capture ratio that characterizes the Zr isotopes; the performance of the n_TOF facility, in particular the high instantaneous flux, allows for neutron-capture measurements on radioactive samples with high accuracy. Table 1 reports the new Zr (n, γ) reaction rates as a function of temperature (in keV) together with the values recommended by Bao et al. (2000) for comparison. The calculation of the MACS was carried out by folding the capture cross section with the thermalized stellar spectra over a wide neutron energy range, starting from ∼100 eV and extending to ∼500 keV, to match the thermal neutron distributions at the highest temperatures reached during shell carbon burning in massive stars. In this context, the n_TOF measurements are limited to a few tens of keV. The MACS resulting from the n_TOF data analysis are composed of a first component calculated directly from the extracted resonance parameters and a second component given by the JENDL calculations (Shibata 2002) at high energy. In the n_TOF measured range, it is possible to extract the ratio between the MACS calculated using n_TOF resonance data and those presented by theoretical evaluations (Shibata 2002; Nakagawa et al. 2005). To complement n_TOF data at higher energies, two different approaches are possible: (1) scale the evaluation by the same factor extracted in

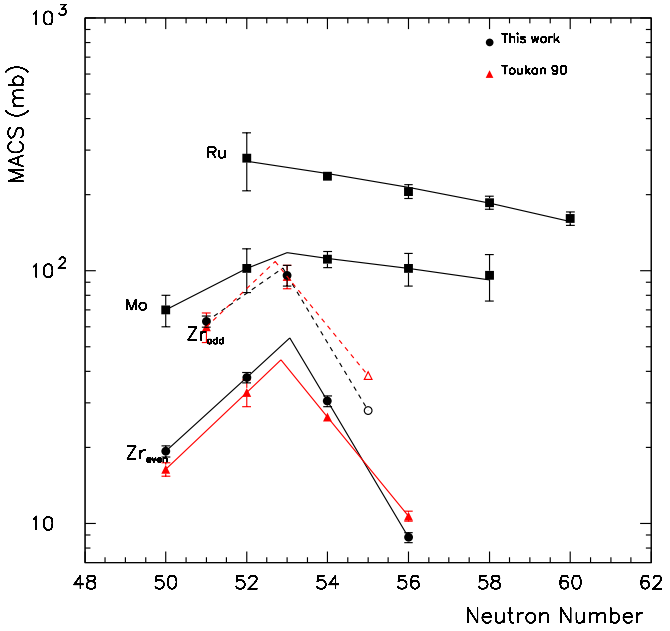

Figure 1. Systematics of the MACS data in the Zr/Mo/Ru region used for determining the MACS of the unstable branch point isotope ^{95}Zr (open symbols with no error bars). Black points represent n_TOF data and our current results, red points are from Toukan & Kaeppeler (1990). Solid and dashed lines connect MACS values of even and odd isotopes, respectively. Note the strong effect of the magic neutron number, $N = 50$.

(A color version of this figure is available in the online journal.)

the n_TOF measured range, or (2) add the contribution at high energy as given by the evaluations. The contribution at high energy becomes important for thermal energies (kT) higher than 30 keV, since the measured range extends at least up to 40 keV. For the scope of this paper (where the stellar temperature never exceeds $kT \sim 30$ keV), the only critical isotope is ^{93}Zr, for which it was possible to extract n_TOF resonance parameters only below 8 keV of incident neutron energy. The data used in the present paper have been derived using approach (1) above. More information on the measurements and data analysis prescription can be found in Tagliente (2008a, 2008b) and Tagliente et al. (2010, 2011a, 2011b, 2013).

In Table 1, we also report our new estimate for the MACS of ^{95}Zr. Because it is not possible to measure the MACS of this short-lived isotope at n_TOF, we derived it using the method of Toukan & Kaeppeler (1990) by applying the trend of the MACS values as a function of neutron number for the even and odd isotopes. The method is illustrated in Figure 1, which shows the strong effect of the magic neutron number, $N = 50$, on the MACS values along the isotope chains of Zr and Mo. Due to the lower MACS measured by n_TOF for ^{96}Zr, we derived a ^{95}Zr$(n,\gamma)^{96}$Zr rate roughly 50% lower than that reported by Toukan & Kaeppeler (1990). When compared to the recommended MACS of Bao et al. (2000), which was obtained on the basis of local systematics, our result is roughly three times lower.

Finally, we note that for the neutron captures on the Zr isotopes, we are in the fortunate situation where the contribution of the laboratory-determined rate to the stellar rate is equal to unity (Rauscher 2012), which means that we can safely use the laboratory rates as the stellar rates and apply an uncertainty equal to the laboratory uncertainties of ∼5% at 1σ (as compared to uncertainties up to ∼13% reported in the Bao et al. 2000 compilation). This is obviously not true for ^{95}Zr(n, γ)^{96}Zr, which was instead derived empirically and thus carries a larger uncertainty, which is difficult to evaluate and could be up to a factor of two.

3. STELLAR MODELS

We performed detailed nucleosynthesis calculations, imposing a post-processing algorithm on previously computed stellar evolutionary sequences. The details of this procedure and the codes used to compute the models have been described in detail by, e.g., Lugaro et al. (2004) and Karakas et al. (2009).

3.1. The Stellar Structure Sequences

We used stellar structure models calculated from the zero-age main sequence to the end of the AGB phase using the Monash Mt Stromlo stellar structure code (Lattanzio 1986) and included mass loss on the AGB phase using the prescription of Vassiliadis & Wood (1993). We only consider models that become C-rich, to allow for the formation of SiC. We considered the 3 $M_\odot$ and 4 $M_\odot$ models of metallicity $Z = 0.02$ from Karakas (2010), the 3 $M_\odot$ model of $Z = 0.01$ from Shingles & Karakas (2013), and the 1.25 $M_\odot$ and 1.8 $M_\odot$ models of metallicity $Z = 0.01$ from Karakas et al. (2010). The $Z = 0.01$ models were computed with the inclusion of the C- and N-rich low-temperature opacity tables from Lederer & Aringer (2009), while the $z = 0.02$ models were not (Karakas 2010). To achieve a C-rich envelope composition, convective overshoot was required in the 1.25 $M_\odot$ and 1.8 $M_\odot$ models. We included overshoot by extending the position of the base of the convective envelope by $N_{\rm ov}$ pressure-scale heights. A C-rich envelope required $0.5 \lesssim N_{\rm ov} \lesssim 5$, depending on the stellar mass: in the 1.25 $M_\odot$ and 1.8 $M_\odot$ models, we set $N_{\rm ov} = 4$ and 3, respectively (for more details, see Karakas et al. 2010). Experimenting with the efficiency of overshoot to change the TDU efficiency when modeling AGB stars is necessary to match observational constraints such as the O- to C-rich transition luminosity in Magellanic Cloud clusters (e.g., Kamath et al. 2012); this is justified because we still lack a reliable description of convective borders in stars. This overshoot has the effect of deepening the TDU but does not lead to the formation of a partially mixed zone in the top layers of the intershell and the consequent ^{13}C pocket because we use instantaneous mixing in the evolutionary code. This is different to the time-dependent convective overshoot used by Herwig (2000) and Cristallo et al. (2009b), which leads to the formation of the ^{13}C pocket, depending on the value of the overshoot parameter β. It is only in the post-processing code that we artificially add a partially mixed zone into the top of the intershell at the deepest extent of each TDU episode to obtain the ^{13}C pocket (see Section 3.2).

The main structural features of these models are presented in Table 2 where we report the following: the stellar mass (Mass, in $M_\odot$) and metallicity (Z) of the model, the number of TPs followed by the TDU (TDUs), the number of TDUs for which C/O > 1 is verified in the envelope (TDUs with C > O), the maximum temperature in the TPs ($T_{\rm TP}^{\rm max}$, in MK), the total mass dredged up by the TDU ($M_{\rm dred}$, in $M_\odot$), the final envelope mass (final $M_{\rm env}$, in $M_\odot$), and the final C/O ratio (final C/O). We select AGB models that become C-rich after a certain number of pulses and do not suffer strong hot bottom burning. For metallicities around solar, this corresponds to a range of masses roughly between 1.5–4 $M_\odot$ (e.g., Groenewegen et al. 1995; Abia et al. 2001; Gail et al. 2009), with the lower limit poorly constrained and perhaps down to 1 $M_\odot$ (Wallerstein & Knapp 1998). For the 1.25 $M_\odot$, 1.8 $M_\odot$, and 3 $M_\odot$ models of

Table 2
Details of Stellar Models

Mass ($M_\odot$)	Z	TDUs	TDUs with C > O	T^{max}_{TPs} (MK)	M_{dred} ($M_\odot$)	Final M_{env} ($M_\odot$)	Final C/O
1.25	0.01	3	2[a]	246	0.013	0.026	2.23[a]
1.8	0.01	6	4[b]	266	0.041	0.014	3.12[b]
3	0.01	16	11	306	0.120	0.004	3.32
3	0.02	16	5[c]	302	0.081	0.676	1.44[c]
4	0.02	15[d]	2[d]	332	0.056	0.958	1.13[d]

Notes.
[a] Using $Z = 0.03$ in the post-processing we obtained 1 TDUs with C > O and final C/O = 1.04.
[b] Using $Z = 0.03$ in the post-processing we obtained 2 TDUs with C > O and final C/O = 1.33.
[c] Using $Z = 0.03$ in the post-processing we obtained 1 TDUs with C > O and final C/O = 1.08.
[d] This model experienced mild hot bottom burning (with a temperature of 23 MK at the base of the convective envelope), which delayed the formation of a C-rich envelope. As discussed in the text, this model may experience two more TDU episodes, which would further increase the C/O ratio.

$Z = 0.01$, it was possible to evolve the models to very small envelope masses and to the end of the AGB (see Table 2). In the case of the 3 $M_\odot$ and 4 $M_\odot$ models of $Z = 0.02$, due to convergence difficulties, we could not evolve the star to the end of the AGB phase (i.e., the final envelope mass is still well above 0.01 $M_\odot$ by the end of the evolution). However, since we are in a phase of very high mass loss ($\sim 10^{-5}$–10^{-4} $M_\odot$ yr^{-1}) we do not expect any further TPs and TDUs to occur for the 3 $M_\odot$ model, and only two further TPs and TDUs to occur for the 4 $M_\odot$ model (Karakas & Lattanzio 2007). Table 2 also shows the maximum temperature achieved at the base of the TPs in each of the models. Recall that the ^{22}Ne neutron source is activated only if this temperature reaches over 300 MK. This means that this neutron source does not operate in the 1.25 $M_\odot$ and 1.8 $M_\odot$ models; it is only marginally active in the 3 $M_\odot$ models and is at work in the 4 $M_\odot$ model, though not enough to produce significant *s*-process enhancements without the introduction of a ^{13}C pocket.

3.2. The Stellar Nucleosynthesis Sequences

The detailed *s*-process nucleosynthesis was calculated using a post-processing code that takes stellar structure information—such as temperature, density, and convective velocity as a function of interior mass and time—and solves implicitly the set of equations that simultaneously describe changes to the model abundances due to mixing and nuclear reactions (Cannon 1993). We assumed scaled solar initial compositions, taking the solar abundances from the compilation by Asplund et al. (2009). These authors derive a solar metallicity of 0.0142, which we rounded to 0.015. According to this value, our stellar structure models cover a metallicity range from 2/3 of solar ($Z = 0.01$) to 4/3 of solar ($Z = 0.02$). We further calculated nucleosynthesis models with a metallicity of $Z = 0.03$ (i.e., 2× solar) using the stellar structure of the $Z = 0.01$ (for the 1.25 $M_\odot$ and 1.8 $M_\odot$) and $Z = 0.02$ (for the 3 $M_\odot$) models, and changing the metallicity at the start of the post-processing. This resulted in a lower number of TDUs with C > O in the envelope and lower final C/O ratios. This approach is not self-consistent, but it is justified as a first approximation for small variations in the metallicity because the *s*-process nucleosynthesis is more sensitive to the metallicity (see discussion in the next section) than the evolutionary sequence is. Comparing, for example, the stellar structure features reported in Table 2 for the 3 $M_\odot$ models of $Z = 0.02$ and $Z = 0.01$, we see that the main difference is in the amount of TDU mass, which is 50% higher in the lower-metallicity model. (As mentioned above, the different final envelope mass is due to numerical instabilities in the 3 $M_\odot$ $Z = 0.02$ model, and we do not expect any further TDU episode for this model.) By keeping the same stellar evolutionary sequence while changing the metallicity within a factor of three in the post-processing code, we are within the model uncertainties because the amount of TDU, which also depends on the stellar lifetime and the uncertain mass-loss rate, is still not well determined in AGB stellar models (Frost & Lattanzio 1996; Mowlavi 1999; Stancliffe & Jeffery 2007; Karakas et al. 2012).

The ^{13}C pocket is included artificially in the post-processing phase by forcing the code to mix a small amount of protons from the envelope into the intershell at the end of each TDU. We simply assume that the proton abundance in the intershell decreases monotonically (and exponentially) from the envelope value of ∼0.7 to a value of 10^{-4} at the given point in the mass that sits below the base of the envelope by an amount of mass "M_{mix}". This method is described in more detail in Lugaro et al. (2004, 2012) and is very similar to that used by Goriely & Mowlavi (2000). We chose $M_{mix} = 0.002\ M_\odot$, which produces a ^{13}C pocket representing ∼1/10–1/20 of the whole intershell. This allows us to reproduce the basic observation that the *s*-process elements in AGB stars of around solar metallicity are enhanced by up to an order of magnitude, with respect to Fe and solar abundances (e.g., Busso et al. 2001). Our results are very close to those obtained by Cristallo et al. (2009b) (see also Section 4), who include the ^{13}C pocket by introducing a velocity profile below the inner border of the convective envelope and set the value of their free parameter β to 0.1; they also do this to reproduce basic observational constraints. In Section 4.2, we present a number of test cases where we changed the M_{mix} parameter as well as the proton profile to investigate its impact on the Zr isotopic ratios.

We employed a network of 320 nuclear species from neutrons and protons up to Bi. Nuclear reaction rates were included using the *reaclib* file provided by the Joint Institute for Nuclear Astrophysics (JINA; Cyburt 2010) as of 2012 May (reaclib_V2.0). The rates of the neutron-source reactions correspond to Heil (2008) for the ^{13}C(α, n)^{16}O and to Iliadis et al. (2010) for the ^{22}Ne(α, n)^{25}Mg and ^{22}Ne(α,γ)^{26}Mg reactions. For the neutron-capture cross sections, the JINA reaclib database includes the KADoNiS database (Dillmann et al. 2006).[11] For the Zr neutron-capture cross sections, we run models using the values from Bao et al. (2000) and from this work (Table 1).

4. RESULTS AND DISCUSSION

Figures 2–4 compare the Zr isotopic composition at the stellar surface of AGB models to the grain data. As mentioned above, the ^{96}Zr/^{94}Zr ratio depends on the neutron density, which is mostly determined by the stellar mass, whereas the other ratios depend on the neutron exposure, which in our models is mostly determined by the stellar metallicity. First, we show and discuss the changes in model predictions

[11] We used the rates labeled as *ka*02 in the JINA database (instead of *kd*02) as they provide the best fits to KADoNiS at the temperature of interest for AGB stars.

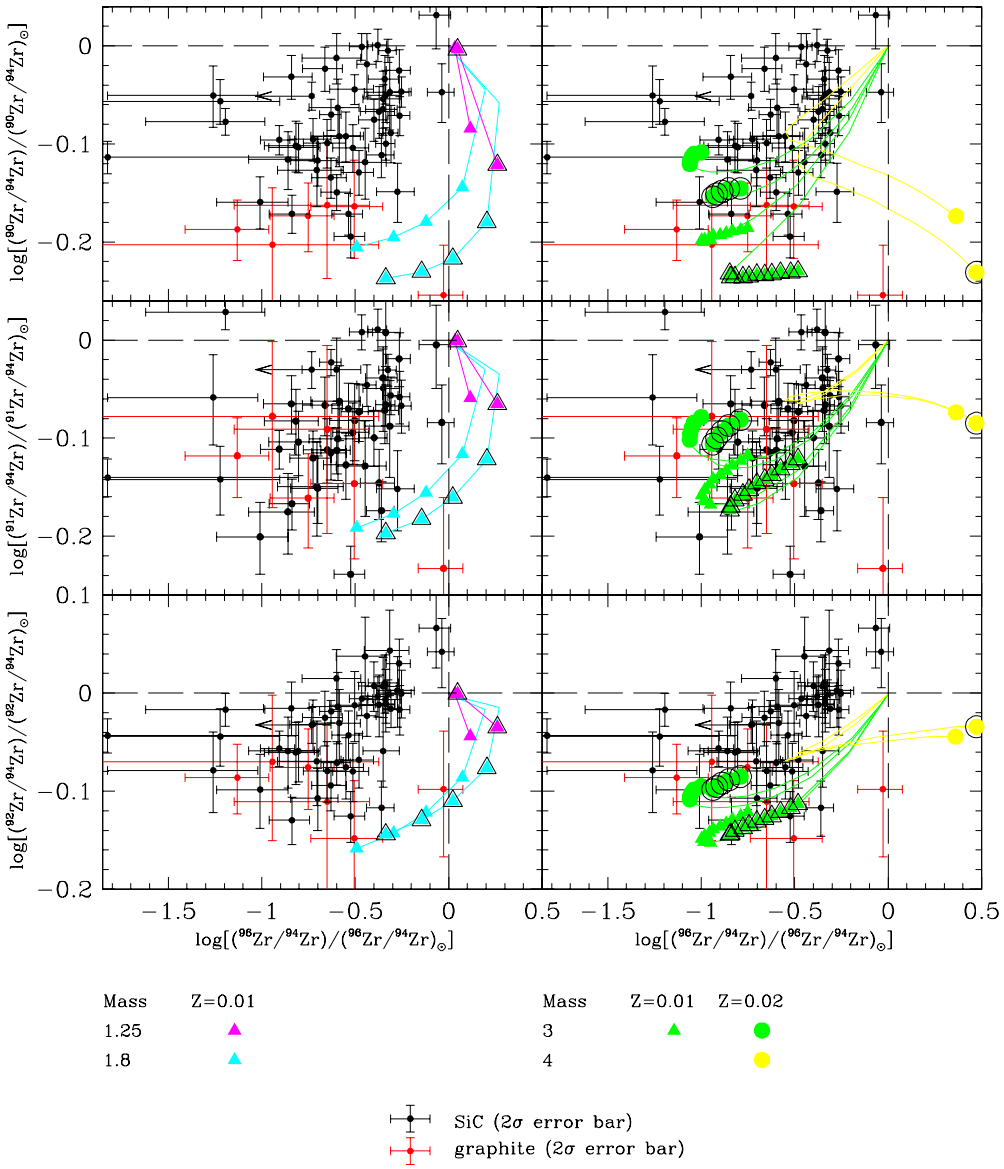

Figure 2. Zr isotopic ratios measured in single SiC grains (Nicolussi et al. 1997; Davis et al. 1998, 1999; Barzyk et al. 2007) and high-density graphite grains (Nicolussi et al. 1998) are compared to those predicted by our AGB models (all computed with $M_{\rm mix} = 0.002\ M_{\odot}$) using MACS values for the Zr isotopes from the present work (symbols without the black contour) and from Bao et al. (2000; symbols with the black contour). The AGB symbols represent the composition at the stellar surface after each TDU episode for which C/O > 1.

(A color version of this figure is available in the online journal.)

driven by the updated Zr neutron-capture cross sections and associated uncertainties. Second, we discuss in detail the mass and metallicity dependencies and their implications, including the impact of the ^{13}C pocket features and of stellar rotation.

4.1. The Impact of the New MACS

Figure 2 presents the Zr isotopic composition at the stellar surface of our five AGB models computed with different sets of MACS for the Zr isotopes as compared to the grain data. The results for the 3 $M_{\odot}$ models computed with the MACS from Bao et al. (2000) present similar trends to the 3 $M_{\odot}$ models shown in Figure 5 of LDG03, even though ^{96}Zr/^{94}Zr does not reach values as high as those produced by the 3 $M_{\odot}$ models presented in LDG03 because there are fewer TPs with C/O > 1 in the envelope. The main reason for this is the different choice of the mass-loss rate, where the mass-loss rate from Vassiliadis & Wood (1993) used here typically results in fewer TPs than the mass-loss from Reimers (1975) used in LDG03. (See Lugaro et al. 2003b and Stancliffe & Jeffery 2007 for comparisons of different 3 $M_{\odot}$ $Z = 0.02$ models.) Using the neutron-capture cross sections from Bao et al. (2000), we found similar problems as already discussed in LDG03 and mentioned in Section 1: the handful of grains with ^{96}Zr/^{94}Zr 10 times lower than solar are not reached by the models and some of the highest ^{90,91,92}Zr/^{94}Zr ratios are also unmatched. We cannot invoke stardust experimental uncertainties as the reason why the models do not cover some of the grains because the plotted measurement error bars are at 2σ. Updating the MACS of the Zr isotopes to the new values presented in Section 2 partly solved the problems above. The lower MACS for ^{95}Zr allows our 3 $M_{\odot}$ models to reach a ^{96}Zr/^{94}Zr lower than one-tenth of solar. On the other hand, even using the new MACS for ^{95}Zr, the 4 $M_{\odot}$ model produces a final ^{96}Zr/^{94}Zr higher than solar, confirming the result of LDG03 that the grains should come from stars of mass

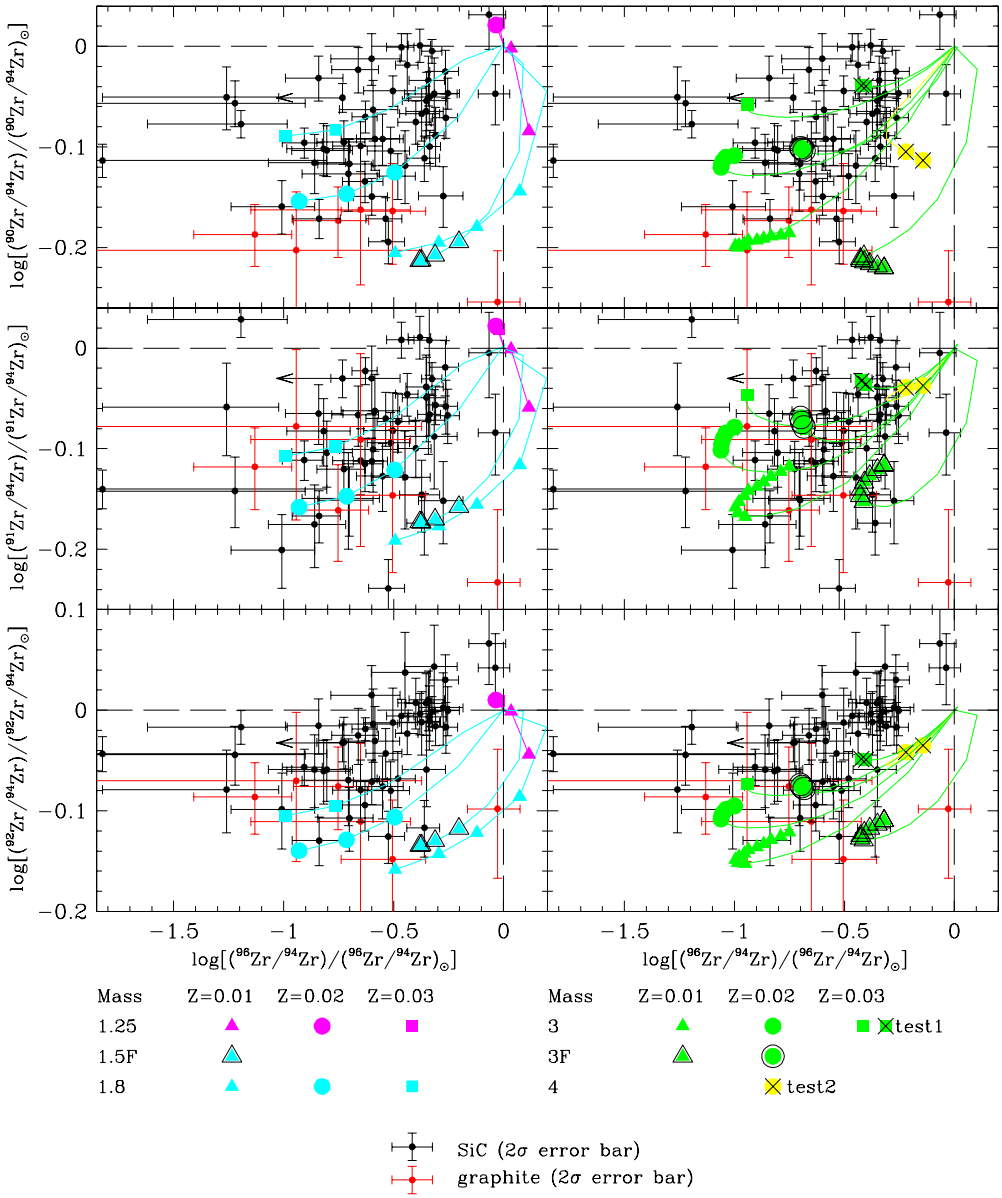

Figure 3. Same as Figure 2, except that all the models are computed using the Zr MACS values from this work and more AGB model predictions are plotted, extending the predictions to higher metallicities, and including results from three models from the FRUITY database (label "F"). All our models were computed using $M_{\rm mix} = 0.002\,M_{\odot}$, except for the cases labeled as "test," which were computed with $M_{\rm mix} = 0.0002\,M_{\odot}$.

(A color version of this figure is available in the online journal.)

up to $\sim$3 $M_{\odot}$. This model will be further discussed in the next section.

The lower MACS for ^{90}Zr allows our models to reach a higher ^{90}Zr/^{94}Zr. For ^{91}Zr/^{94}Zr, no major change results, whereas for ^{92}Zr/^{94}Zr, the match with the data is slightly worse. It is still not possible to match the large fraction of grains with ^{92}Zr/^{94}Zr around solar, unless we consider $\sim$10% uncertainties (at 2σ) associated with the new MACS. When multiplying the MACS by a factor between 0.9 and 1.1, the isotopic ratios vary linearly with the change in the MACS. For example, when we multiply the MACS of ^{92}Zr by 0.9, we obtain a 1.1 times higher value for ^{92}Zr/^{94}Zr (+0.04 in the Figure 2 log scale); when we multiply the MACS of ^{92}Zr by 0.9 and at the same time multiply the MACS of ^{94}Zr by 1.1, we obtained a 1.2 times higher value for ^{92}Zr/^{94}Zr (+0.08 in the Figure 2 log scale); and so on. This rule holds for all Zr isotopes except ^{96}Zr, which is much more sensitive to the MACS of ^{95}Zr and did not show any significant variations when varying its MACS within 10%.

The MACS of ^{93}Zr is particularly interesting; since the radioactive decay of ^{93}Zr leads to the stable ^{93}Nb, it determines the production of mono-isotopic Nb. The value presented here is not significantly changed from Bao et al. (2000), and we confirm the results of LDG03 for the elemental Zr and Nb abundances used by Kashiv et al. (2010) for comparison to the SiC data.

Finally, when considering the effect of nuclear physics inputs, it should be kept in mind that many other reactions that involve light elements may also have some effect on the neutron exposure from the ^{13}C neutron source. This is due to (1) changes in the abundances of both the ^{13}C nuclei and the light neutron-poison nuclei (e.g., ^{14}N) and (2) to the recycling of the protons produced by the ^{14}N(n, p)^{14}C reaction, as discussed in detail by Lugaro et al. (2003b). For example, the ^{12}C(p, γ)^{13}N reaction

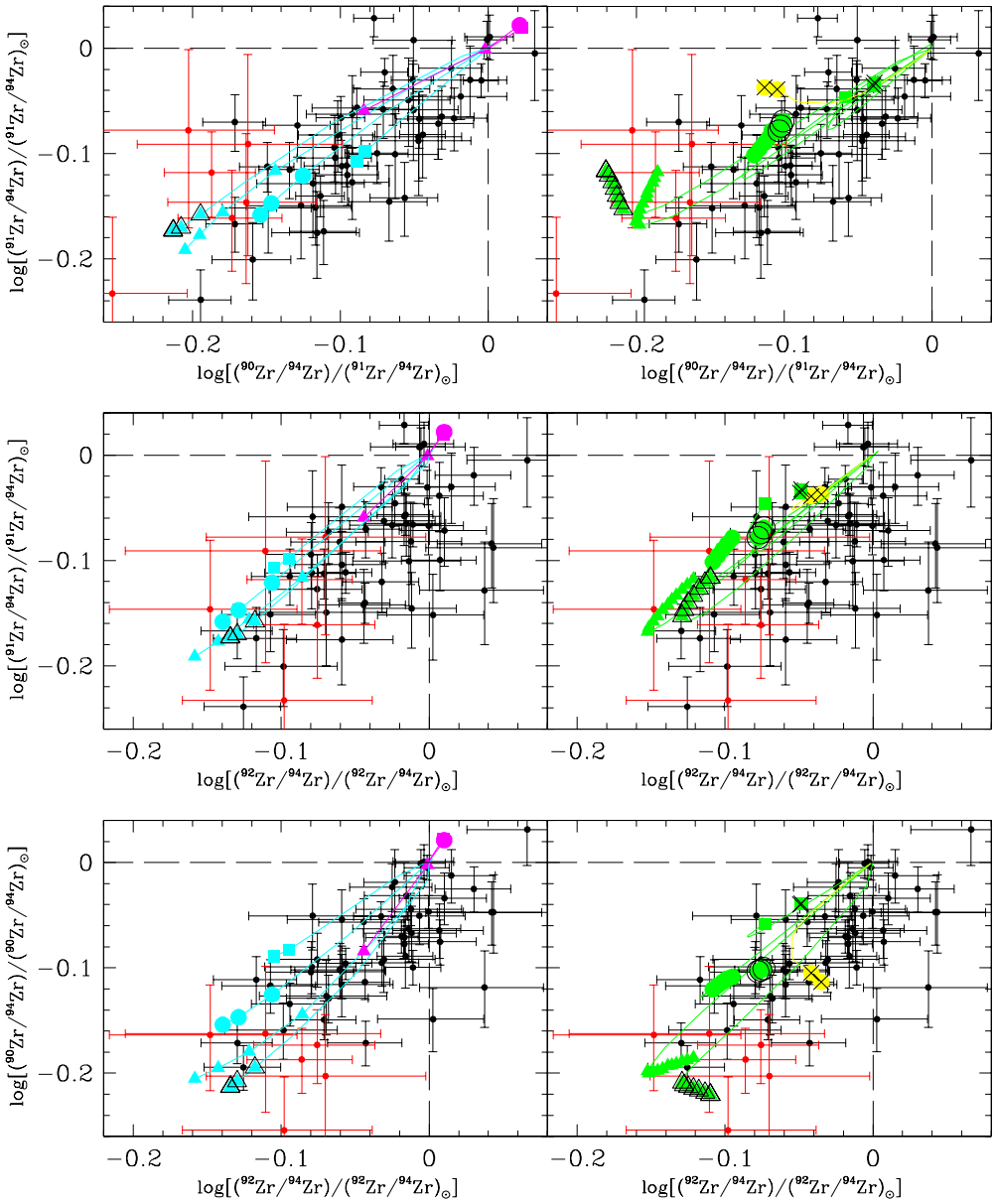

Figure 4. Same as Figure 3, except that the isotopic ratios ^{90,91,92}Zr/^{94}Zr are plotted against each other.
(A color version of this figure is available in the online journal.)

rate in the JINA reaclib_V2.0 database is updated to the value given by Li et al. (2010). This rate is up to 20% higher than the NACRE rate (Angulo et al. 1999) and produces up to 10% lower ^{90,91,92}Zr/^{94}Zr ratios (−0.04 in the Figure 2 log scale), depending on the model, due to a higher abundance of ^{13}C in the pocket.

4.2. The Impact of New AGB Models

Figure 3 presents a number of AGB models computed with the new MACS in comparison to the grain data and similar models from the FRUITY database (Cristallo et al. 2011). Overall, we find a very good agreement between our models and the FRUITY models, with the differences most likely due to different MACS and to the fact that the extent of the ^{13}C pocket is kept constant in our models, while it decreases with the pulse number in the FRUITY models (Cristallo et al. 2009b). For a self-consistency check, in Figure 4, we present the same data and models as in Figure 3, but plot ^{90,91,92}Zr/^{94}Zr against each other in the three possible combinations. This plot highlights the composition of one unusual grain with a ^{91}Zr/^{94}Zr higher than solar that cannot be reached by any of the models.

4.2.1. The Effect of the Stellar Mass

As mentioned in Section 1.1.2, the ^{96}Zr/^{94}Zr ratio depends on the activation of the ^{95}Zr branching point. This is a function of the neutron density, which in turn is a function of the mass. In the 3 $M_{\odot}$ and 4 $M_{\odot}$ models, ^{96}Zr/^{94}Zr decreases during the first TDU episodes and then increases during the final TDUs due to the higher temperatures, leading to marginal activation of the ^{22}Ne neutron source. In the 3 $M_{\odot}$ models, the last computed TP reaches 302 MK and 305 MK for metallicities $Z = 0.02$ and $Z = 0.01$, respectively; in the 4 $M_{\odot}$ model, it reaches 332 MK (see Table 2), with the last 8 TPs experiencing temperatures in excess of 300 MK in this model. The surface ^{24}Mg/^{25}Mg ratio, which can be taken as a quantitative indicator of the activation

of the ^{22}Ne neutron source, changes in the 4 $M_{\odot}$ model from the initial solar value of 7.9 to a value in the range 5.9–6.8, depending on the adopted $M_{\rm mix}$; this is because ^{14}N in the pocket adds to the ^{22}Ne amount in the intershell. In the 3 $M_{\odot}$ models, ^{24}Mg/^{25}Mg changes to 6.6–7.2 (at $Z = 0.01$) and 7.3–7.6 (at $Z = 0.02$).

The opposite happens in the 1.25 $M_{\odot}$ and 1.8 $M_{\odot}$ models because the ^{22}Ne neutron source is never activated (the ^{24}Mg/^{25}Mg ratio remains solar); however during the first TPs, the ^{13}C pocket is engulfed in the TPs instead of burning during the interpulse periods (Section 1.1.1, point 1). For example, during the interpulse period following the first TDU episode of the 1.8 $M_{\odot}$ model, the temperature at the location of the ^{13}C pocket reaches only 76 MK. This behavior has also been reported by Cristallo et al. (2009b) for their 2 $M_{\odot}$ stellar model at solar metallicity. The result is a higher neutron density produced by the ^{13}C neutron source in the first phases of the evolution, e.g., 1.2×10^9 cm^{-3} in the TP following the first TDU episode of the 1.8 $M_{\odot}$ model, which results in a ^{96}Zr/^{94}Zr higher than solar. After the first few TPs of the 1.8 $M_{\odot}$ model, ^{13}C burns radiatively, producing low neutron densities; and the ^{96}Zr/^{94}Zr moves toward values lower than solar. In the lowest-mass model presented here (1.25 $M_{\odot}$), most of the ^{13}C nuclei burn after they are ingested in the TP, which results in low neutron exposures and a close-to-solar *s*-process composition.

We can conclude that the grains showing the lowest values of the ^{96}Zr/^{94}Zr ratios (lower than one-tenth solar) are best explained by models with masses between 1.8 $M_{\odot}$ and 3 $M_{\odot}$. We stress that this conclusion is possible only thanks to our updated MACS for ^{95}Zr and that, unfortunately, the uncertainties in the MACS for ^{95}Zr are still significant. We should also keep in mind that the possible inclusion of overshoot at the base of the TP convective region (Section 1.1.1, point 3) would lead to an increase of the efficiency of the ^{95}Zr branching point (Lugaro et al. 2003b), shifting the mass range determined here. The significant number of more mildly ^{96}Zr-depleted grains, with ^{96}Zr/^{94}Zr ~1/3–1/2 of solar (−0.5 to −0.3 in the Figure 3 log scale), can be interpreted as a result of either (1) the activation of the ^{22}Ne neutron source in stars of mass >3 $M_{\odot}$, or (2) the lower *s*-process production due to the lower neutron exposure associated with the ^{13}C pocket ingested in the TP in stars of mass between 1.25 $M_{\odot}$ and 1.8 $M_{\odot}$. The clear lack of grains with a ^{96}Zr/^{94}Zr between solar and one-half of solar can potentially be used to infer the maximum or the minimum mass of a C-rich star within scenarios (1) or (2), respectively. Case (2) would have implications on point 1 of Section 1.1.1: because the 1.25 $M_{\odot}$ model sits close to solar composition, it appears to be ruled out as the site of origin for the majority of the grains, and we would need a minimum mass for C-rich stars (of roughly solar metallicity) between 1.25 $M_{\odot}$ and 1.8 $M_{\odot}$ in order to overcome the gap and match the grains at ^{96}Zr/^{94}Zr ~ 1/2 solar. On the other hand, the 1.25 $M_{\odot}$ model represents a potential explanation for the two grains with a ^{96}Zr/^{94}Zr close to solar. A similar conclusion was reached by Ávila et al. (2013a) in relation to the Ba composition of extremely large (~5–20 μm) SiC grains. In this case, compositions close to solar may be related to specific conditions for the formation of the lowest-mass C-rich stars.

4.2.2. The ^{13}C-pocket Uncertainties

When we decreased $M_{\rm mix}$ by a factor of 10 (i.e., $M_{\rm mix} = 0.0002\,M_{\odot}$) in the 3 $M_{\odot}$ $Z = 0.03$ model, we found another possible solution for the grains with ^{96}Zr/^{94}Zr ~1/3–1/2 of solar ("test1" in Figure 3). Such a solution related to varying $M_{\rm mix}$ would favor a stochastic process for the formation of the ^{13}C pocket. However, this process would have to be fine tuned to avoid producing grains with ^{96}Zr/^{94}Zr ratios between solar and one-half of solar, where the data show the clear gap discussed above. We also note that applying the same $M_{\rm mix}$ choice to the 4 $M_{\odot}$ model, we obtained ^{96}Zr/^{94}Zr ratios lower than solar ("test2" in Figure 3). The difference between this case and the $M_{\rm mix} = 0.002\,M_{\odot}$ case, which produced ^{96}Zr/^{94}Zr ratios higher than solar (see Figure 2), is due to lower amounts of ^{14}N in the mixing zone, which is ingested in the TPs and converted into ^{22}Ne. Note that if no ^{13}C pocket is introduced in the 4 $M_{\odot}$ model, the Zr isotopic ratios remain solar within 1%.

We also considered models where we investigated the effect of introducing different profiles of protons to produce the ^{13}C pocket. As explained in Section 3, in all the models presented so far, we have assumed that the proton abundance included below the base of the convective envelope at the end of each TDU decreases exponentially (i.e., as 10^{-x}, where x is the depth in mass) from the envelope value of ~0.7 to a value of 10^{-4} at $M_{\rm mix} = 0.002\,M_{\odot}$ below the base of the envelope. When we changed the proton profile to follow the exponential of $x^{1/3}$, $x^{1/2}$, x^2, and x^3, instead of x, we did not find any significant changes in the Zr isotopic ratios for the 3 $M_{\odot}$ $Z = 0.02$ model. All the variations were well within the nuclear uncertainties discussed in the previous section. We then assumed that the proton abundance decreases exponentially starting from values ranging from 0.5 to 0.001, i.e., lower than the envelope value of 0.7. We found significant differences only when the starting value was decreased to 0.001, in which case ^{90,96}Zr/^{94}Zr increased by 20%, (+0.08 in the Figure 3 log scale).

4.2.3. The Effect of Stellar Metallicity and Rotation

As mentioned in Section 1.1.2, the isotopic ratios involving ^{90,91,92}Zr, being close to the magic number of neutrons ($N = 50$), depend on the neutron exposure produced by the ^{13}C neutron source. Because this neutron source is primary, i.e., it is produced starting from the H and He initially present in the star, it is well known that its neutron exposure is ~$^{13}C/Z$ (Clayton 1988; Gallino et al. 1998). Thus, varying either the amount of ^{13}C, as done in LDG03, or the stellar metallicity, as done here, results in variations in the neutron exposure and in ^{90,91,92}Zr/^{94}Zr. Specifically, the ^{90,91,92}Zr/^{94}Zr ratios increase by increasing the metallicity or decreasing the amount of ^{13}C. We are encouraged in our approach of varying the metallicity instead of the amount of ^{13}C by the fact that the six graphite grains showing the Zr *s*-process signature are better matched by models of AGB stars of metallicity lower than solar, which have already been identified as the stellar sources of some low-density graphite grains on the basis of their Ne (Heck et al. 2009) and Kr (Amari 2003) compositions. We also note that the metallicity range of the grain parent stars derived here from their Zr composition is in agreement with that derived from their Si composition (Lewis et al. 2013). Furthermore, the metallicity range considered here is well determined from the models: stars with metallicity higher than $Z \sim 0.03$ do not become C-rich, whereas stars with metallicity lower than $Z \sim 0.01$ produce the same Zr isotopic ratios as the $Z = 0.01$ models. This is because below such metallicity, the first bottleneck at the N = 50 magic number of neutrons is always bypassed and the Zr isotopic ratios behave asymptotically.

We tested some 3 $M_{\odot}$, $Z = 0.02$ stellar models where we allowed the neutron exposure in the ^{13}C to vary more freely, as it

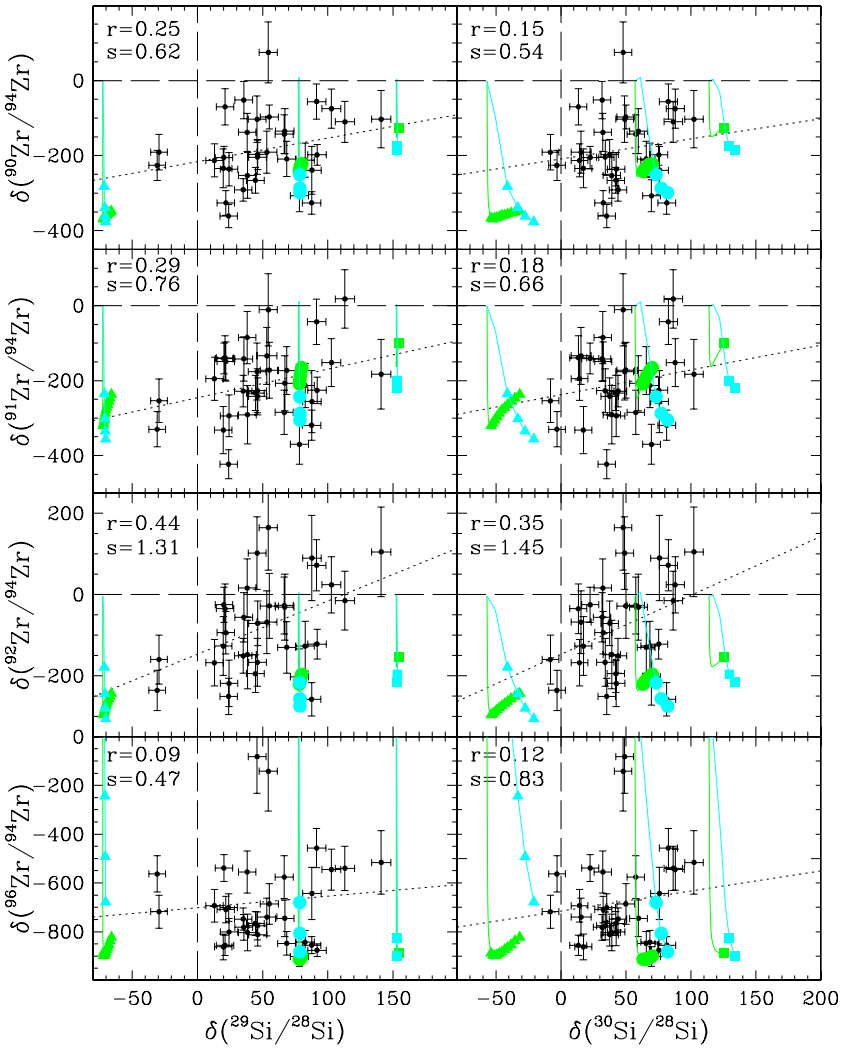

Figure 5. All possible combinations of $\delta(^{90,91,92,96}Zr/^{94}Zr)$ vs. $\delta(^{29,30}Si/^{28}Si)$ from the SiC data set of Barzyk et al. (2007, black symbols with 2σ error bars). The data linear regression lines are plotted as dotted lines, with their slopes and correlation coefficients indicated in each panel as "*s*=" and "*r*=," respectively. The 1.8 $M_{\odot}$ (cyan symbols) and 3 $M_{\odot}$ (green symbols) models of metallicities $Z = 0.01$ (triangles), 0.02 (circles), and 0.03 (squares) are also plotted, where we assumed different initial $\delta(^{29,30}Si/^{28}Si)$ values for each different metallicity to account for the chemical evolution of the Galaxy (Lewis et al. 2013).

(A color version of this figure is available in the online journal.)

could happen due to the impact of stellar rotation. As mentioned in Section 1.1.1 (point 2), the potential effect of stellar rotation is to lower the neutron exposure (Herwig et al. 2003; Siess et al. 2004; Piersanti et al. 2013). Clearly, changing the initial velocity of any given stellar model, as well as considering the effect of, e.g., magnetic fields, would allow for a wide range of neutron exposures. We simulated them by running a set of models in which we assumed a constant abundance of protons mixed from the base of the convective envelope down to $M_{\rm mix} = 0.002\ M_{\odot}$ below it to allow for the formation of the ^{13}C pocket. We tested a wide range of proton abundances, from 10^{-4} to 0.05. These tests allowed us to cover, with just one mass and one metallicity, a range of Zr isotopic ratios similar to that predicted by our whole set of models; LDG03 achieved a similar result by varying the ^{13}C-pocket efficiency. We also note that the higher neutron exposures resulting from overshoot at the base of the convective pulse (Section 1.1.1, point 3) would require rotation to lower the neutron exposure and reproduce the observed spread (Herwig et al. 2003). The question is how can we discriminate between the effect of metallicity and the effect of rotation and determine which is the primary effect in shaping the stardust Zr distribution?

One way to answer this question is provided by considering the $^{29,30}Si/^{28}Si$ ratios of stardust. These ratios increase with the stellar metallicity (Figure 2 of Lewis et al. 2013) because they are mostly determined by the initial composition of the star, which in turn is a function of metallicity via the chemical evolution of the Galaxy. However, they do not depend on stellar rotation. This means that possible positive correlations between the $^{90,91,92}Zr/^{94}Zr$ and $^{29,30}Si/^{28}Si$ ratios can provide us with a quantitative proxy for the effect of metallicity. Note that we do not expect strong correlations between $^{96}Zr/^{94}Zr$ and any of the $^{29,30}Si/^{28}Si$ ratios because $^{96}Zr/^{94}Zr$ does not strongly depend on the metallicity (see Figure 3). The effect of rotation can then be derived by considering the spread of $^{90,91,92}Zr/^{94}Zr$ ratios around such possible positive correlations, though it should be kept in mind that these correlations are also smeared out in $^{29,30}Si/^{28}Si$ by the effect of possible small inhomogeneities in

the interstellar medium, which can shift the initial $^{29,30}Si/^{28}Si$ ratios by ∼7% for any given metallicity (Lugaro et al. 1999; Nittler 2005).

In Figure 5, we plot the Zr ratios as function of the Si ratios for the 32 available single SiC grains from Barzyk et al. (2007) and indicate the slopes their correlation coefficients of their regression lines. In this plot, we use the δ notation where

$$\delta(^{i}Zr/^{94}Zr) = (((^{i}Zr/^{94}Zr)/(^{i}Zr/^{94}Zr)_{\odot}) - 1) \times 1000)$$

represents the permil variation of the given ratio with respect to the solar ratio (so that $\delta = 0$ represents solar ratios and, e.g., $\delta = +500‰$ means a ratio 50% higher than solar). For comparison, we also plot our AGB predictions for 1.8 $M_{\odot}$ and 3 $M_{\odot}$ stars and different metallicities with initial Si isotopic ratios shifted to account for the chemical evolution of the Galaxy as reported by Lewis et al. (2013).

The positive correlations produced by the effect of metallicity are hinted at by the small set of currently available data, particularly in $^{92}Zr/^{94}Zr$ versus $^{29}Si/^{28}Si$, which suggests that the effect of metallicity is predominant. That a correlation should be more evident in $^{92}Zr/^{94}Zr$ versus $^{29}Si/^{28}Si$ is expected because $^{30}Si/^{28}Si$ is known to be more affected by AGB nucleosynthesis, as shown in Figure 5 (see also Zinner et al. 2006), and the $^{90,91}Zr/^{94}Zr$ ratios may also be changed by the branching points at the unstable $^{89,90}Sr$ and ^{91}Y. It seems difficult to disentangle the effect of inhomogeneities in the interstellar medium on $^{29}Si/^{28}Si$ from the possible secondary effect of rotation on $^{92}Zr/^{94}Zr$ in producing the spread around the regression line. Future work may involve superposing a random choice of initial $^{29}Si/^{28}Si$ values, as expected by inhomogeneities. Also, as already noted in Section 4.1, the $^{92}Zr/^{94}Zr$ ratios are not well fitted by the models. This point will need to be reinvestigated in the light of new determinations of the MACS of ^{92}Zr.

5. CONCLUSIONS

We have compared the Zr isotopic composition derived from stellar models of C-rich AGB stars with masses of 1.25–4 $M_{\odot}$ and metallicities of 0.01–0.03, including updated MACS for the Zr isotopes, to the composition of Zr measured in stardust SiC and graphite grains. Our main conclusions can be summarized as follows.

1. The new Zr MACS measurements and our new evaluation of the MACS of the unstable branching point nucleus ^{95}Zr allow a good match to the SiC and graphite data within the nuclear uncertainties; however, the predicted $^{92}Zr/^{94}Zr$ values are, on average, still outstandingly lower than the data points. To address this problem, new measurements of the MACS of ^{92}Zr have been performed at n_TOF and at the linear electron accelerator facility GELINA (Belgium); these data are currently being analyzed. Furthermore, new measurements for the MACS of ^{93}Zr for a wide energy range have been carried out at n_TOF, which will allow us to avoid the use of theoretical models for a more accurate determination of the MACS of this isotope; these data are also currently being analyzed.
2. From analysis of the $^{96}Zr/^{94}Zr$ ratios, we confirm the results of LDG03 that stellar masses below 4 $M_{\odot}$ are the best candidates for the origin of the vast majority of the mainstream SiC grains and conclude that the most ^{96}Zr-depleted grains must originate from stars of mass ∼1.8–3 $M_{\odot}$. However, we cannot unambiguously attribute a mass to the more mildly ^{96}Zr-depleted grains as they can be explained by both higher and lower masses. Measurements of other isotopic ratios affected by branching points (such as $^{86}Kr/^{82}Kr$ and $^{134}Ba/^{136}Ba$) in the same grain will provide independent constraints to settle this question. Because possible overshoot at the base of the convective TP would change the picture outlined here, more models that consider this effect are needed. Our lowest-mass C-rich stellar model (1.25 $M_{\odot}$) may be a suitable site of origin for the two grains with close-to-solar Zr composition (see also Ávila et al. 2013a).
3. We find that the spread in neutron exposures needed to produce the range of observed $^{90,91,92}Zr/^{94}Zr$ isotopic ratios can be naturally produced by considering the same range of metallicities ($Z = 0.01$–0.03) needed to explain the Si isotopic composition of the grains, as derived from Galactic chemical evolution models (Lewis et al. 2013). If this interpretation is correct, other effects, such as stochastic variations in the proton profile that lead to the formation of the ^{13}C pocket or stellar rotation, would play a secondary role. To verify this point we investigated the correlations between the $^{90,91,92}Zr/^{94}Zr$ and $^{29,30}Si/^{28}Si$ isotopic ratios in the available 32 data points from Barzyk et al. (2007) and found a hint that metallicity is the predominant effect.

Other elements measured in SiC may be expected to present similar correlations as the Zr and Si isotopic ratios discussed in the last item above. Specifically, ratios involving nuclei with a magic number of neutrons—such as $^{88}Sr/^{86}Sr$, $^{138}Ba/^{136}Ba$, and $^{208}Pb/^{204}Pb$—should correlate with isotopic ratios of elements affected by the chemical evolution of the Galaxy, such as Si and Ti. Ba and Si ratios are available for 20 grains from Barzyk et al. (2007). These together with two new Ba/Si studies of over 100 grains to be published shortly by two of us (Savina and Davis) will be considered in a forthcoming paper. Marhas et al. (2007) analyzed Ba and Si in another 16 grains; however, these analyses were performed with the NanoSIMS instrument (Zinner et al. 2001) and may suffer from molecular interferences (Ávila et al. 2013b). While the number of grains analyzed for both Sr, Zr, or Ba and Si or Ti data is quite limited at present, measurements of Sr, Ba, and Si isotopes in a suite of grains are currently underway using the Resonance Ionization Mass Spectrometer CHARISMA (Savina et al. 2003) and the NanoSIMS. Furthermore, thanks to the upcoming CHicago Instrument for Laser Ionization (CHILI) at the University of Chicago (Stephan et al. 2013), much more high-precision data will become available in the near future, which will be fundamental in determining if the spread in the Zr isotopic ratios in SiC and graphite is primarily due to a metallicity effect. At the same time, asteroseismology observations of white dwarfs (e.g., Charpinet et al. 2009) and red giant stars (Mosser et al. 2012) are providing us with evidence that the cores of red giant and AGB stars spin much more slowly than expected by simple models of the evolution of the angular momentum in stars and that strong coupling between the core and the envelope is required to match the observations (Suijs et al. 2008; Tayar & Pinsonneault 2013). A slower-rotating core would also lead to a smaller impact of rotation on the neutron exposure in the ^{13}C pocket. More quantitative studies are required, which together with the upcoming extended sample of grain data from CHILI and CHARISMA will set firm constraints on the operation of the *s*-process in AGB stars.

We thank Mark van Raai and Robin Humble for support on the post-processing code. We thank Peter Hoppe for discussion on grain data. We acknowledge the constructive criticism of the anonymous referee, who greatly helped us to improve the structure, focus, and clarity of the paper. M.L. and A.I.K. are grateful for the support of the NCI National Facility at the ANU. M.L. is an ARC Future Fellow (supported by grant FT100100305). A.I.K. is an ARC Future Fellow (supported by grant FT10100475). This work was partially supported by the National Aeronautics and Space Administration, through grants to A.M.D. and M.R.S. The CHARISMA instrument at Argonne National Laboratory is supported by the US Department of Energy, BES Division of Materials Science and Engineering, under contract DEAC02-06CH11357.

REFERENCES

Abia, C., Busso, M., Gallino, R., et al. 2001, ApJ, 559, 1117
Amari, S. 2003, PASA, 20, 378
Angulo, C., Arnould, M., Rayet, M., et al. 1999, NuPhA, 656, 3
Arlandini, C., Käppeler, F., Wisshak, K., et al. 1999, ApJ, 525, 886
Asplund, M., Grevesse, N., Sauval, A. J., & Scott, P. 2009, ARA&A, 47, 481
Ávila, J. N., Ireland, T. R., Gyngard, F., et al. 2013a, GeCoA, 120, 628
Ávila, J. N., Ireland, T. R., Lugaro, M., et al. 2012a, *Lunar Planet. Sci.*, Vol. 43 (League City, TX: LPI), 2709
Ávila, J. N., Ireland, T. R., Lugaro, M., et al. 2013b, ApJL, 768, L18
Ávila, J. N., Lugaro, M., Ireland, T. R., et al. 2012b, ApJ, 744, 49
Bao, Z. Y., Beer, H., Käppeler, F., et al. 2000, ADNDT, 76, 70
Bartolome, Z. M., Hockenbury, R. W., Moyer, W. R., Tatarczuk, J. R., & Block, R. C. 1969, NSE, 37, 137
Barzyk, J. G., Savina, M. R., Davis, A. M., et al. 2007, M&PS, 42, 1103
Bernatowicz, T., Fraundorf, G., Ming, T., et al. 1987, Natur, 330, 728
Bisterzo, S., Gallino, R., Straniero, O., Cristallo, S., & Käppeler, F. 2010, MNRAS, 404, 1529
Boldeman, J. W., Allen, B. J., de, L., Musgrove, A. R., & Macklin, R. L. 1975, NuPhA, 246, 1
Boldeman, J. W., de, L., Musgrove, A. R., Allen, B. J., Harvey, J. A., & Macklin, R. L. 1976, NuPhA, 269, 31
Boothroyd, A. I., Sackmann, I.-J., & Ahern, S. C. 1993, ApJ, 416, 762
Borcea, C., Cennini, P., Dahlfors, M., et al. 2003, NIMPA, 513, 524
Busso, M., Gallino, R., Lambert, D. L., Travaglio, C., & Smith, V. V. 2001, ApJ, 557, 802
Busso, M., Gallino, R., & Wasserburg, G. J. 1999, ARA&A, 37, 239
Cannon, R. C. 1993, MNRAS, 263, 817
Charpinet, S., Fontaine, G., & Brassard, P. 2009, Natur, 461, 501
Clayton, D. D. 1988, MNRAS, 234, 1
Clayton, D. D. 2003, ApJ, 598, 313
Clayton, D. D., & Nittler, L. R. 2004, ARA&A, 42, 39
Coceva, P., Giacobbe, P., & Magnani, M. 1979, in Proc. of the Conf. on Nucl. Cross Sections for Technology in Knoxville (Washington, DC: US Dept. of Commerce), 319
Cristallo, S., Piersanti, L., Straniero, O., et al. 2009a, PASA, 26, 139
Cristallo, S., Piersanti, L., Straniero, O., et al. 2011, ApJS, 197, 17
Cristallo, S., Straniero, O., Gallino, R., et al. 2009b, ApJ, 696, 797
Croat, T. K., Stadermann, F. J., & Bernatowicz, T. J. 2005, ApJ, 631, 976
Cyburt, R. H., Amthor, A. M., Ferguson, R., et al. 2010, ApJS, 189, 240
Davis, A. M. 2011, PNAS, 108, 19142
Davis, A. M., Nicolussi, G. K., Pellin, M. J., Lewis, R. S., & Clayton, R. N. 1998, in Proceedings of the V international symposium on Nuclei in the Cosmos, ed. N. Prantzos & S. Harissopulos (Gif-sur-Yvette: Editions Frontieres), 563
Davis, A. M., Pellin, M. J., Lewis, R. S., Amari, S., & Clayton, R. N. 1999, in Lunar and Planetary Inst. Technical Report, Vol. 30, Lunar and Planetary Institute Science Conference Abstracts (Houston: LPI), 1976
Dillmann, I., Heil, M., Käppeler, F., et al. 2006, in AIP Conf. Ser. 819, Capture Gamma-Ray Spectroscopy and Related Topics, ed. A. Woehr & A. Aprahamian (Melville, NY: AIP), 123
D'Orazi, V., Campbell, S. W., Lugaro, M., et al. 2013, MNRAS, 433, 366
Frost, C. A., & Lattanzio, J. C. 1996, ApJ, 473, 383
Gail, H.-P., Zhukovska, S. V., Hoppe, P., & Trieloff, M. 2009, ApJ, 698, 1136
Gallino, R., Arlandini, C., Busso, M., et al. 1998, ApJ, 497, 388
Gallino, R., Busso, M., & Lugaro, M. 1997, in AIP Conf. Ser. 402, Astrophysical Implications of the Laboratory Study of Presolar Materials, ed. E. K. Zinner & T. J. Bernatowicz (Melville, NY: AIP), 115
Gallino, R., Busso, M., Picchio, G., & Raiteri, C. M. 1990, Natur, 348, 298
Goriely, S. 1999, A&A, 342, 881
Goriely, S., & Mowlavi, N. 2000, A&A, 362, 599
Groenewegen, M. A. T., van den Hoek, L. B., & de Jong, T. 1995, A&A, 293, 381
Guo, B., Li, Z. H., Lugaro, M., et al. 2012, ApJ, 756, 193
Heck, P. R., Amari, S., Hoppe, P., et al. 2009, ApJ, 701, 1415
Heil, M. e. a. 2008, PhRvC, 78, 025803
Herwig, F. 2000, A&A, 360, 952
Herwig, F. 2005, ARA&A, 43, 435
Herwig, F., Langer, N., & Lugaro, M. 2003, ApJ, 593, 1056
Herwig, F., Pignatari, M., Woodward, P. R., et al. 2011, ApJ, 727, 89
Herwig, F., Woodward, P. R., Lin, P.-H., Knox, M., & Fryer, C. 2013, arXiv:1310.4584
Hoppe, P., & Ott, U. 1997, in AIP Conf. Ser. 402, Astrophysical Implications of the Laboratory Study of Presolar Materials, ed. T. J. Bernatowicz & E. Zinner (Melville, NY: AIP), 27
Iliadis, C., Longland, R., Champagne, A. E., Coc, A., & Fitzgerald, R. 2010, NuPhA, 841, 31
Jadhav, M., Amari, S., Marhas, K. K., et al. 2008, ApJ, 682, 1479
Kamath, D., Karakas, A. I., & Wood, P. R. 2012, ApJ, 746, 20
Karakas, A., & Lattanzio, J. C. 2007, PASA, 24, 103
Karakas, A. I. 2010, MNRAS, 403, 1413
Karakas, A. I., Campbell, S. W., & Stancliffe, R. J. 2010, ApJ, 713, 374
Karakas, A. I., García-Hernández, D. A., & Lugaro, M. 2012, ApJ, 751, 8
Karakas, A. I., van Raai, M. A., Lugaro, M., Sterling, N. C., & Dinerstein, H. L. 2009, ApJ, 690, 1130
Kashiv, Y., Davis, A. M., Gallino, R., et al. 2010, ApJ, 713, 212
Larson, N. M. 2006, Report ORNL/TM-9179/R7 (Oak Ridge: Oak Ridge National Laboratory)
Lattanzio, J. C. 1986, ApJ, 311, 708
Lederer, M. T., & Aringer, B. 2009, A&A, 494, 403
Lewis, K. M., Lugaro, M., Gibson, B. K., & Pilkington, K. 2013, ApJL, 768, L19
Li, Z., Su, J., Guo, B., et al. 2010, ScChG, 53, 658
Lugaro, M. 2005, Stardust from Meteorites/Maria Lugaro, Vol. 9 (Singapore: World Scientific)
Lugaro, M., Davis, A. M., Gallino, R., et al. 2003a, ApJ, 593, 486
Lugaro, M., Herwig, F., Lattanzio, J. C., Gallino, R., & Straniero, O. 2003b, ApJ, 586, 1305
Lugaro, M., Karakas, A. I., Stancliffe, R. J., & Rijs, C. 2012, ApJ, 747, 2
Lugaro, M., Ugalde, C., Karakas, A. I., et al. 2004, ApJ, 615, 934
Lugaro, M., Zinner, E., Gallino, R., & Amari, S. 1999, ApJ, 527, 369
Marhas, K. K., Hoppe, P., & Ott, U. 2007, M&PS, 42, 1077
Merrill, S. P. W. 1952, ApJ, 116, 21
Mosser, B., Goupil, M. J., Belkacem, K., et al. 2012, A&A, 548, A10
Mowlavi, N. 1999, A&A, 344, 617
Musgrove, A. R. D. L., Boldeman, J. W., Allen, B. J., Harvey, J. A., & Macklin, R. L. 1977, AuJPh, 30, 391
Nakagawa, T., Chiba, S., Hayakawa, T., & Kajino, T. 2005, ADNDT, 91, 77
Nicolussi, G. K., Davis, A. M., Pellin, M. J., et al. 1997, Sci, 277, 1281
Nicolussi, G. K., Pellin, M. J., Lewis, R. S., et al. 1998, ApJ, 504, 492
Nittler, L. R. 2005, ApJ, 618, 281
Piersanti, L., Cristallo, S., & Straniero, O. 2013, ApJ, 774, 98
Pignatari, M., Herwig, F., Hirschi, R., et al. 2013a, arXiv:1307.6961
Pignatari, M., Wiescher, M., Timmes, F. X., et al. 2013b, ApJL, 767, L22
Plag, R., Heil, M., Käppeler, F., et al. 2003, NIMPA, 496, 425
Rauscher, T. 2012, ApJL, 755, L10
Reimers, D. 1975, in Circumstellar Envelopes and Mass Loss of Red Giant Stars, ed. B. Baschek, W. H. Kegel, & G. Traving (New York: Springer), 229
Rubbia, C., Andriamonje, S. A., Bouvet-Bensimon, D., et al. 1998, Tech. Rep. CERN/LHC/98-02 (Geneva: CERN)
Savina, M. R., Davis, A. M., Tripa, C. E., et al. 2004, Sci, 303, 649
Savina, M. R., Pellin, M. J., Tripa, C. E., et al. 2003, GeCoA, 67, 3215
Shibata, K., Kawano, T., Nakagawa, T., et al. 2002, JNST, 39, 1125
Shingles, L. J., & Karakas, A. I. 2013, MNRAS, 431, 2861
Siess, L., Goriely, S., & Langer, N. 2004, A&A, 415, 1089
Smith, V. V., & Lambert, D. L. 1989, ApJL, 345, L75
Sneden, C., Cowan, J. J., & Gallino, R. 2008, ARA&A, 46, 241
Speck, A. K., Hofmeister, A. M., & Barlow, M. J. 1999, ApJL, 513, L87
Stancliffe, R. J., Dearborn, D. S. P., Lattanzio, J. C., Heap, S. A., & Campbell, S. W. 2011, ApJ, 742, 121
Stancliffe, R. J., & Jeffery, C. S. 2007, MNRAS, 375, 1280
Stephan, T., Pellin, M. J., Rost, D., et al. 2013, LPICo, 1719, 2536
Straniero, O., Gallino, R., & Cristallo, S. 2006, NuPhA, 777, 311

Suijs, M. P. L., Langer, N., Poelarends, A.-J., et al. 2008, A&A, 481, L87
Tagliente, G., Fujii, K., Milazzo, P. M., et al. 2008a, PhRvC, 77, 035802
Tagliente, G., Milazzo, P. M., Fujii, K., et al. 2008b, PhRvC, 78, 045804
Tagliente, G., Milazzo, P. M., Fujii, K., et al. 2010, PhRvC, 81, 055801
Tagliente, G., Milazzo, P. M., Fujii, K., et al. 2011a, PhRvC, 84, 015801
Tagliente, G., Milazzo, P. M., Fujii, K., et al. 2011b, PhRvC, 84, 055802
Tagliente, G., Milazzo, P. M., Fujii, K., et al. 2013, PhRvC, 87, 014622
Takahashi, K., & Yokoi, K. 1987, ADNDT, 36, 375
Tayar, J., & Pinsonneault, M. H. 2013, ApJL, 775, L1
Toukan, K. A., & Kaeppeler, F. 1990, ApJ, 348, 357
Travaglio, C., Gallino, R., Amari, S., et al. 1999, ApJ, 510, 325
Travaglio, C., Gallino, R., Arnone, E., et al. 2004, ApJ, 601, 864
Truran, J. W., & Iben, I., Jr. 1977, ApJ, 216, 797
van Raai, M. A., Lugaro, M., Karakas, A. I., García-Hernández, D. A., & Yong, D. 2012, A&A, 540, A44
Vassiliadis, E., & Wood, P. R. 1993, ApJ, 413, 641
Wallerstein, G., & Knapp, G. R. 1998, ARA&A, 36, 369
Zinner, E. 2008, PASA, 25, 7
Zinner, E., Amari, S., Messenger, S., et al. 2001, M&PSA, 36, 231
Zinner, E., Nittler, L. R., Gallino, R., et al. 2006, ApJ, 650, 350